Modified Polar Format Algorithm for Processing Spaceborne SAR Data

Curtis W. Chen
Jet Propulsion Laboratory, California Institute of Technology
4800 Oak Grove Drive
Pasadena, CA 91109-8099
curtis.chen@jpl.nasa.gov

Abstract—**This paper describes a modified polar format algorithm for SAR image-formation processing. The algorithm focuses raw data assuming a spherical reference surface (ground surface), and, unlike standard polar format algorithms, it assumes spherical rather than planar signal wavefronts. The algorithm, or some variant of it based on the same geometry, might be suitable for spaceborne sensors for which there is significant curvature of the platform flight track and/or curvature of the Earth surface. The algorithm might also provide better phase preservation properties than standard polar format algorithms for applications such as SAR interferometry.**

I. Introduction

We present a modified polar format algorithm for processing spaceborne synthetic aperture radar (SAR) data. The derivation of this algorithm is based upon the geometry of a spherical reference surface (*i.e.*, a spherical Earth) and a platform flight trajectory that can include significant radial curvature, corresponding to the first-order curvature of an orbiting spacecraft. The algorithm may therefore be more accurate than the traditional polar format algorithm for situations in which the geometry of the sensor and the target scene are more appropriately described by a spherical model than a planar model.

The traditional polar format algorithm is well known for processing spotlight-mode SAR data [1], [2]. This algorithm involves the assumption that the spherical wavefronts of the radar pulses can be approximated by planar wavefronts around a central reference point in the imaged scene. The surface to which data are focused is also assumed to be planar when compensating for platform motion. While these approximations are often quite good for small target scenes imaged by airborne platforms, for larger scenes, the approximations might lead to errors in parts of the scene far away from the central reference point. These errors may be of particular concern for applications such as interferometry, in which the image phase as well as the image magnitude must be faithfully reproduced during image-formation processing.

Like the traditional polar-format algorithm, the modified algorithm we present here is based upon the Projection Slice Theorem [3]. The planar projections assumed by the modified algorithm arise not from an assumption of the far-field planarity of the signal wavefronts, however, but from the planarity of the intersections of the spherical wavefronts with a spherical reference surface. The modified algorithm thus begins with a space-domain resampling of the range-compressed pulse data, followed by transform-domain polar reformatting and inverse Fourier transformation. The resulting image is the projection of the reference-surface brightness distribution onto a plane.

In this paper, we describe the principles and basic processing steps of the modified algorithm, then we present results of the application of the algorithm to real spaceborne SAR data from the NASA SIR-C instrument.

II. Algorithm Principles

Define an Earth body-fixed (*i.e.*, rotating) Cartesian coordinate system (see Fig.1) such that the origin is at the Earth center and the positive z axis points towards the SAR location at a reference time $t = 0$. Define an image projection plane to be the plane containing both the z axis and the SAR velocity vector $\vec{v}$ at $t = 0$. Let the positive x axis point in the direction of the component of $\vec{v}$ perpendicular to the z axis at $t = 0$ (the positive x axis points exactly in the direction of the SAR velocity vector at $t = 0$ if the orbit is circular). For some unit vector $\vec{u}$, define the angles β and γ by

$$u_x = \cos\beta \sin\gamma \tag{1}$$

$$u_y = \sin\beta \tag{2}$$

$$u_z = \cos\beta \cos\gamma \tag{3}$$

where u_x, u_y, and u_z are the x, y, and z components of $\vec{u}$. In other words, β is the angle of $\vec{u}$ out of the x-z plane, and γ is the angle of the projection of $\vec{u}$ onto the x-z plane with respect to the z axis. Let r be the distance from the origin of a given point in 3-D space.

We begin by examining the ideal case in which the SAR follows a circular orbit of radius a around a spherical, non-rotating Earth. That is, the SAR flight path is completely in the x-z plane, and there is no Earth surface topography; assume that the SAR look direction is into the $+y$ half-space, corresponding to a left-looking sensor. We neglect any atmospheric or ionospheric effects, and we also assume that there is no SAR motion between the time of pulse transmission and reception.

For a given SAR location, contours of constant range ρ form spheres centered at the SAR location. The intersection of a constant-range sphere with the sphere of the Earth surface is a circle which lies in a plane orthogonal to the SAR position

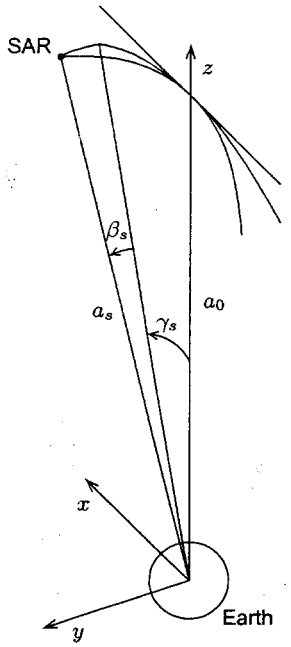

Fig. 1. Earth-centered, rotating (x, y, z) and (r, β, γ) coordinate systems, defined with respect to the SAR position and velocity vectors at time $t = 0$.

vector (see Fig. 2). Let r be the perpendicular distance from the origin to such a plane for a fixed SAR location and a fixed range ρ. From Fig. 3 and the (Cartesian) law of cosines,

$$r = R_E \cos\alpha = \frac{a^2 + R_E^2 - \rho^2}{2a}. \tag{4}$$

Note that the algorithm can be generalized to handle elliptical orbits by varying the orbital radius a for each pulse.

For the ideal case, the algorithm begins with a 1-D space-domain resampling of the range-compressed complex data $d_{0s}(\rho)$ from each pulse. The pulse data should *not* have been motion compensated to a central reference point as is typical in spotlight-mode polar-format SAR processing. The resampling performed here maps slant range ρ to radial distance r according to Eq (4). If all targets are located on the reference sphere, this resampling is exact, as contours of constant range ρ coincide with contours of constant radial distance r. Let the resampled pulse data be denoted $d_{1s}(r)$.

Suppose that for a given pulse, the SAR location—of which we assume perfect knowledge—is $(r = a, \beta = 0, \gamma = \gamma_s)$ where a is the orbit radius, assumed for now to be constant. The subscript 's' denotes that the subscripted variable describes a specific SAR position s along the flight path. All scatterers within a plane orthogonal to the SAR position vector at some perpendicular distance r from the origin contribute to the value of $d_1(r)$. In other words, the value of $d_1(r)$ is the integral over a 2-D plane of the 3-D brightness distribution. The Projection-Slice Theorem [3] therefore implies that $d_1(r)$ contains only Fourier components of the brightness distribution $g(x, y, z)$ along a line in 3-D Fourier space:

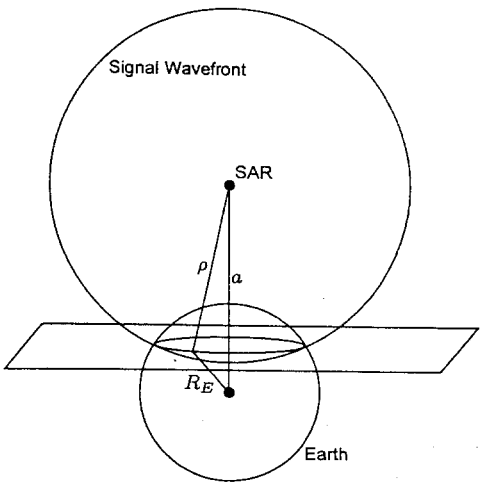

Fig. 2. The intersection of the spherical reference surface with a spherical contour of constant range from the SAR is a circle. With the origin at the Earth center, the circle is contained in a plane perpendicular to the position vector of the SAR.

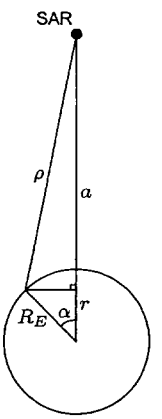

Fig. 3. Relationship of the radial distance r to the slant range ρ and the Earth-central angle α for the ideal case. Note that if a and R_E were to scale in this figure, the spacecraft would be in a medium Earth orbit (MEO) with a period of approximately 12 hours.

$$\int_{-\infty}^{\infty}\left[\int_{-\infty}^{\infty}\int_{-\infty}^{\infty} g(x', y', z')\,\mathrm{d}y'\mathrm{d}z'\right]\exp(-j2\pi u'x')\,\mathrm{d}x' = \left[G(u', v', w')|_{v'=0, w'=0}\right] \tag{5}$$

where

$$G(u', v', w') = \int_{-\infty}^{\infty}\int_{-\infty}^{\infty}\int_{-\infty}^{\infty} g(x', y', z') \times \exp(-j2\pi(u'x' + v'y' + w'z'))\,\mathrm{d}x'\mathrm{d}y'\mathrm{d}z'. \tag{6}$$

While given here only for one direction in the arbitrary (x', y', z') coordinate system, the theorem generalizes to all directions through the rotation property of the Fourier transform. In words, Eqs. (5) and (6) state that the 1-D Fourier transform

of a 2-D projection integral of a distribution is a 1-D line through the 3-D Fourier transform of the distribution along the same direction as the projection. This can be explained intuitively by noting that the projection integrals filter out all sinusoidal components whose wavefronts are not parallel to the planes of integration, as those components cycle equally through positive and negative values and hence result in zero upon integration.

Using the Projection-Slice Theorem, we can therefore estimate the original brightness distribution using tomographic techniques. Let f_x, f_y, f_z, and f_r be the frequency-domain (Fourier-transform) variables associated with the space-domain variables x, y, z, and r, with the forward Fourier transform defined through Eq. (6). Let γ and β be defined for the frequency domain just as they are for the spatial domain. The 1-D Fourier transform $D_1(f_r)$ of $d_1(r)$ is thus a line sample of the 3-D Fourier transform $G(f_x, f_y, f_z)$ of the desired 3-D brightness distribution $g(x, y, z)$, along the line in the frequency domain defined by γ_s, still assuming $\beta = 0$. That is,

$$D_1(f_r) = G(f_x = f_r \sin\gamma_s, f_y = 0, f_z = f_r \cos\gamma_s). \quad (7)$$

Because the SAR position vector does not leave the $\beta = 0$ plane (by our assumption of the simple motion model used for this section), the frequency-domain data lie exclusively in the f_x-f_z plane. The collected data are therefore insensitive to spatial brightness variations in the y direction, and the 2-D inverse Fourier transform of the frequency data in the f_x-f_z plane gives the projection of the brightness data onto the x-z plane. We denote this projected data $g(x, z)$.

The modified polar format algorithm thus entails a 1-D Fourier transform over the variable r for each resampled pulse return, then a 2-D inverse Fourier transform over the frequency-domain variables f_x and f_z. This 2-D inverse transform requires a polar-to-Cartesian resampling of the frequency-domain data if Fast Fourier Transform (FFT) techniques are to be used. For efficiency, the 2-D interpolation step can be implemented as two 1-D interpolations; furthermore, one of these 1-D interpolation steps can be incorporated into the $\rho \rightarrow r$ resampling.

For the ideal case, the recovered projection is exact, assuming that no errors are introduced during interpolation. Furthermore, because all scatterers are assumed to lie on the reference sphere, the recovered brightness data can be projected uniquely from the x-z plane back onto the reference sphere, or onto whatever output coordinate system is desired. (This assumes that the SAR antenna rejects all signals from the $-y$ half space.)

In the literature of traditional spotlight SAR and polar format algorithms [1], [2], the along-track resolution depends on the angular extent of the aperture as viewed from the target. This angle determines the width of the annular section of the signal energy's region of support in the frequency domain. In our modified algorithm, however, the width of the region of support is equal to the angular extent of the aperture as viewed from the Earth center, as the origin of the coordinate system is not near the target. Bearing in mind that the effective wavelength is scaled when mapping ρ to r, though, the along-track resolution may still be derived in a self-consistent manner using a frequency-domain analysis.

This section has so far assumed the simplified case of a perfectly spherical, nonrotating Earth. A more realistic case, of course, requires that we consider both Earth topography and the platform relative motion out of the $\beta = 0$ plane due to Earth rotation. These effects, if significant, will cause errors in the $\rho \rightarrow r$ resampling of the simplified description above and will therefore degrade the image focus. We will not discuss the details of compensating for these effects here, however. It suffices to note that motion-compensation techniques can, to first order, correct for small departures of the platform from the $\beta = 0$ plane. (Motion within the $\beta = 0$ plane, even if noncircular, can be compensated exactly with the algorithm by allowing a to vary for each pulse.)

Note that for the ideal case, the continuous-time derivation above is independent of the along-track antenna pointing direction (or changes in it), so the basic geometry of the algorithm can be used for processing SAR data acquired in either stripmap mode, spotlight mode, or a hybrid strimpmap-spotlight mode. The algorithm might also be well suited to the task of processing burst-mode (ScanSAR data). In real systems, the discrete nature of the data requires that sampling issues be addressed and that different acquisition modes be handled differently, however. These issues are below.

III. Sampling

The previous section has dealt mainly with the continuous-variable derivation of the modified polar-format algorithm. In this section, we address issues related to the discrete nature of SAR data.

A. Range Sampling

After range compression, the first major processing step of the proposed algorithm is the $\rho \rightarrow r$ resampling of the pulse data. Assuming that the received data are sampled adequately in time, and hence equivalently sampled in slant range ρ, the spacing Δr of the resampled data can be chosen so that the data are adequately sampled in r as well:

$$\Delta r \leq \Delta\rho \left(\left. \frac{\mathrm{d}r_s}{\mathrm{d}\rho_s} \right|_{\rho=\rho_{0s}} \right). \quad (8)$$

Note that the near edge of the radar swath dictates Δr because this is where samples in ρ will be most compressed in the $\rho \rightarrow r$ resampling.

Generally, the sampled pulse data will be offset from the origin and will have been downconverted to baseband from a high-frequency carrier f_c. Let $\tilde{d}_{0s}(\tilde{\rho})$ be the offset, downconverted signal, such that

$$\tilde{d}_{0s}(\tilde{\rho}) = d_{0s}(\rho) \exp(-j2\pi f_{\rho c}\rho) \quad (9)$$

where $\tilde{\rho} = \rho - \rho_0$ and $f_{\rho c} = f_c(2/c_0)$, with c_0 being the speed of light.

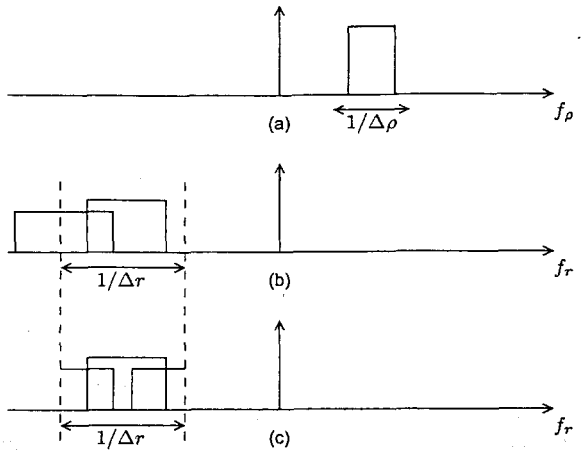

Fig. 4. Point target spectra: (a) as a function of the slant-range frequency f_ρ; (b) as a function of the radial distance frequency f_r; (c) as a function of f_r and aliased into the sampled bandwidth, given by $1/\Delta r$.

The resampled signal as a function of r will also be offset from the origin and will likely also be downconverted from a carrier f_{rcs}, where, as above, the subscript s denotes that the carrier may vary with the pulse. The resampled signal is thus given by

$$\begin{aligned} \tilde{d}_{1s}(\tilde{r}) &= d_{1s}(r)\exp(-j2\pi f_{rcs}r) \\ &= \tilde{d}_{0s}(\tilde{\rho})\exp(j2\pi(f_{\rho c}\rho - f_{rcs}r)). \end{aligned} \quad (10)$$

(11)

This expression implies that in implementation, the offsets must be accounted for in determining the data sample locations (as in the ω-k algorithm [4]), and a phase term must be applied after resampling to reinsert the carrier $f_{\rho c}$ and to remove the carrier f_{rcs}. It might be natural to choose the f_r carrier from

$$f_{rcs} = f_{\rho c}\left(\left.\frac{\mathrm{d}\rho}{\mathrm{d}r}\right|_{\rho=\rho_{\mathrm{mid}}}\right) \quad (12)$$

where ρ_{mid} is the midswath slant range. To first order (*i.e.*, if $\beta_s = 0$),

$$\frac{\mathrm{d}r_s}{\mathrm{d}\rho_s} \approx -\frac{\rho_s}{a_s}, \quad (13)$$

so f_{rcs} normally has the opposite sign as $f_{\rho c}$. Moreover, because the resampling is not uniform across the swath, the center of a target's spectrum will change after resampling (see Fig. 4). That is, depending upon the range of point target, the degree to which the spectrum of the target will be stretched and its carrier frequency scaled will vary.

As the center of the chirp spectrum varies, it is possible that the spectrum will wrap within the sampled bandwidth. This can be avoided by oversampling the data in r or by dividing the range swath into multiple subswaths with different carriers f_{rcs}. A chirp z-transform approach [5] may also be viable (this will be the subject of future work). If the subswath approach is chosen, the subswaths can be made relatively short, as the resampling operation is not performed until after range compression. In fact, it may be desirable to partition the swath into multiple subswaths in order to use short FFTs during the subsequent parts of the algorithm. Spectral wrapping is most problematic as the chirp fractional bandwidth decreases and the fractional swath width (*i.e.*, the ratio of the swath width to the midswath slant range) increases.

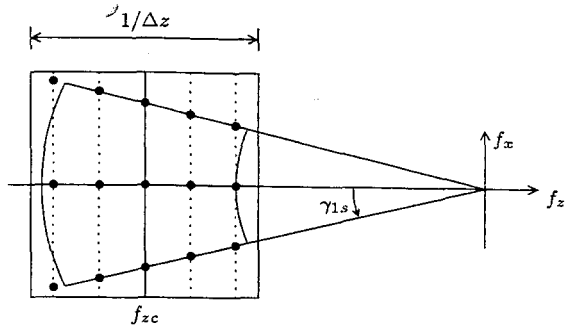

Fig. 5. Fourier transform of radially resampled data. When the pulses are resampled as described in the text, their 1-D Fourier transforms form a 'keystone' as shown when laid out at their respective angles γ_{1s}. The frequency samples of each resampled pulse transform are evenly spaced in f_z and centered on f_{zc}.

In implementation, the 2-D frequency-domain polar-to-Cartesian resampling operation can be performed as two sets of 1-D interpolations, with the first interpolation carried out on the spectrum of each pulse. For efficiency, this interpolation step can be carried out in the space domain and incorporated into the algorithm's $\rho \rightarrow r$ resampling (see Fig. 5). In order to do so, the sample spacing Δr_s for a given pulse should be chosen through

$$\Delta r_s = \Delta z \cos(\gamma_{1s}) \quad (14)$$

where Δz is a selected output pixel spacing in the z direction; Δz should be small enough that Eq. (8) is satisfied everywhere. The carrier f_{rcs} for each pulse used in Eq. (11) should be chosen through

$$f_{rcs} = \frac{f_{zc}}{\cos(\gamma_{1s})} \quad (15)$$

where f_{zc} is a selected reference carrier. If all the echoes have the same number of points, the transforms of the discrete data will be sampled at the same positions in f_z, as is desired in preparation for azimuth resampling.

B. Azimuth Sampling

An analysis of data sampling in the along-track direction depends upon the mode of SAR operation. Regardless of the chosen processing algorithm, however, the radar instrument must operate at a pulse repetition frequency (PRF) that is high enough to sample the instantaneous received Doppler spectrum. We now derive this condition from the frequency-domain framework of the proposed algorithm.

Assuming that γ does not vary much over the aperture and that there is little squint, it is evident from Fig. 5 that the

frequency-domain sample spacing in the f_x direction is given by

$$\Delta f_x = -f_z \Delta\gamma. \tag{16}$$

A sample spacing Δf_x in the frequency domain gives a spatial extent x_{ext} in the space domain given by

$$x_{\text{ext}} = \frac{1}{\Delta f_x} = -\frac{1}{f_z \Delta\gamma}. \tag{17}$$

Because $f_z \approx f_r$, substitution from Eq. (12) gives

$$x_{\text{ext}} = -\frac{1}{f_\rho \left(\frac{\mathrm{d}r}{\mathrm{d}\rho}\right) \Delta\gamma}, \tag{18}$$

and substitution from Eq. (13) gives

$$x_{\text{ext}} = \frac{1}{f_\rho (a/\rho)\Delta\gamma} = \frac{\rho/f_\rho}{a\Delta\gamma}. \tag{19}$$

The slant range frequency f_ρ is equal to the inverse of half the radar wavelength $\lambda/2$, and $a\Delta\gamma = \Delta x$, so

$$x_{\text{ext}} = \frac{\rho(\lambda/2)}{\Delta x}. \tag{20}$$

The width of the antenna footprint, given by $\rho(\lambda/L)$ where L is the antenna length, should be less than x_{ext} in order to avoid ambiguities:

$$x_{\text{ext}} = \frac{\rho(\lambda/2)}{\Delta x} \geq \rho\frac{\lambda}{L}, \tag{21}$$

or

$$\Delta x \leq \frac{L}{2}. \tag{22}$$

This is the well-known result that the distance that the radar moves between pulses must be less than half the antenna length if the instantaneous Doppler spectrum is to be adequately sampled. The centroid of the Doppler spectrum depends on the antenna pointing direction, however.

In terms of our frequency-domain analysis, the spectra of point scatterers are multiplied by linear phase terms in the f_x direction depending on their x coordinates with respect to the reference coordinate frame. The derivation above shows that the f_x sampling rate is sufficient to separate the instantaneous responses of scatterers within a width x_{ext}, but if the scatterers are all displaced from the z axis by an amount x_c, their spectra will be mixed with a complex carrier. The manner with which this carrier is dealt depends on the SAR mode. We now examine the specific case of spotlight-mode acquisition.

Ideally in spotlight SAR, the same limited region ('spot') on the ground is illuminated for the duration of the acquisition (*i.e.*, over the entire synthetic aperture). The spot may be offset from from the z axis by an amount x_c due to antenna squint, but we assume that x_c is known from information about the antenna pointing or can be determined through an examination of the data.

In this mode of operation, the frequency domain data are simply the 2-D Fourier transform of the desired brightness distribution, mixed with a complex carrier $\exp(-j2\pi f_x x_c)$. This carrier may be removed with the multiplication of the conjugate complex exponential before azimuth resampling, the effect of which is to shift the space-domain coordinate system by an amount x_c. Inverse Fourier transformation then yields the desired brightness distribution for an extent x_{ext} about a scene center x_c. Fig. 6 shows a block diagram of the various processing steps required.

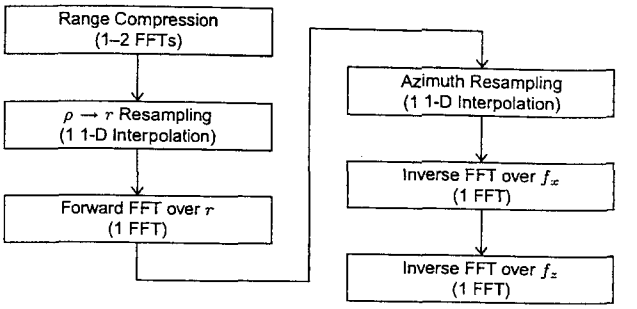

Fig. 6. Block diagram summarizing the major processing steps of the proposed algorithm.

IV. Example Data

This section illustrates the results of applying the proposed algorithm to spotlight-mode SAR data from the NASA SIR-C radar flown on the Space Shuttle Endeavor. The data shown here were acquired of Sydney, Australia and surrounding regions on 30 September 1994 from an altitude of 223 km. During this datatake, the instrument acquired both C- and L-band data in both VV and VH polarizations. The synthetic aperture lengths for both frequencies correspond to an angular extent of 1.5° when viewed from the ground, giving along-track resolutions of 1.1 m and 4.6 m for the C- and L-band channels. The pulse bandwidth is 20 MHz for both frequencies, leading to slant and ground range resolutions of 7.5 and 11 m.

The images produced by the algorithm appear to be well focused, although no corner reflectors or calibration targets were found in the data. The urban areas imaged during the datatake contain a large number of bright, point-like targets, but most of the targets examined were not sufficiently discrete (*i.e.*, point like) for evaluating the performance of the processor. That is, while many features appear point like at low resolution, closer inspection of the data reveals that these features are at least somewhat distributed in space. Thus, although the results are promising, the performance of the processor cannot be verified completely from this data set. Earlier application of the algorithm to simulated point-target data (not shown) gave excellent results, however.

Except where noted, all images presented in this section are shown in the output coordinate system of the processor. This coordinate system maps the brightness distribution of the assumed spherical reference surface—nominally, the local Earth surface—onto the x-z plane. The processor nominally outputs the images such that slant-range increases from left to right, though the horizontal pixel spacing is still constant in z rather than in slant range ρ.

Fig. 7. Portion of the L-band VV image of Sydney Bay. The image is flipped such that range increases towards the left in order to more closely match natural ground coordinates.

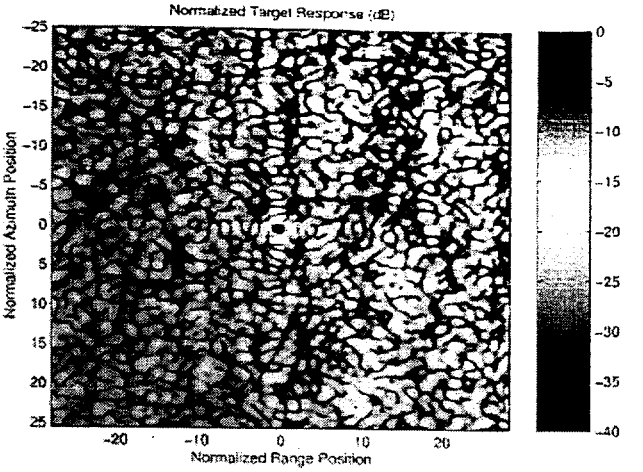

Fig. 8. Normalized, upsampled response of a selected target from a C-band VV image of the datatake.

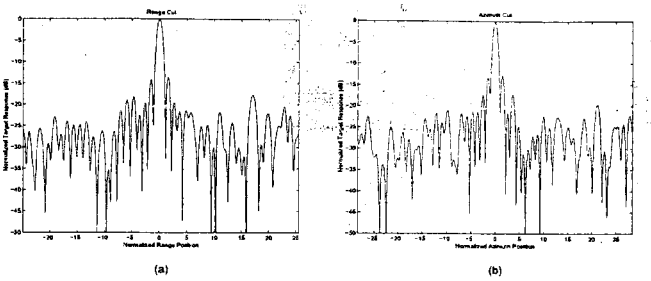

Fig. 9. Cuts through the target response of Fig. 8: (a) range response; (b) azimuth response.

Fig. 7 shows a portion of the L-band VV image containing Sydney Bay. The image is arranged such that range increases towards the left in order to more closely match natural ground coordinates. North is towards the upper right.

Fig. 8 shows an upsampled portion of a C-band VV image from the datatake. The bright scatterer shown behaves almost like a point target, but it is only somewhat stronger than the surrounding area. Cuts through the response of this target are shown in Fig. 9; the -3 dB widths of the target-response main lobe in both dimensions are within a few per cent of the expected resolutions for the system. The first sidelobes in both cuts are at approximately -13 dB, as expected from the uniform spectral weighting used during processing. Unfortunately, because the target is not bright enough compared to its background, a more detailed evaluation of the target sidelobe structure is not possible.

Note that while much of the original motivation of this work was to investigate the phase-preservation properties of the proposed algorithm, we have not performed any analysis on the phase behavior of the SIR-C results. The algorithm offered predictable phase behavior on simulated point-target data, however.

V. Conclusions

We have presented a modified polar-format algorithm for processing SAR data. The algorithm may be well suited to cases in which there is significant curvature of the platform trajectory and/or the reference surface, and it may also offer better phase-preservation properties for applications such as SAR interferometry.

Acknowledgment

This work was performed at the Jet Propulsion Laboratory, California Institute of Technology, under a contract with the National Aeronautics and Space Administration.

References

[1] W. G. Carrara, R. S. Goodman, and R. M. Majewski, *Spotlight Synthetic Aperture Radar: Signal Processing Algorithms*, (Artech House, Boston, 1995).

[2] C. V. Jakowatz, Jr., D. E. Wahl, P. H. Eichel, D. C. Ghiglia, and P. A. Thompson, *Spotlight-Mode Synthetic Aperture Radar: A Signal Processing Approach*, (Kluwer, Boston, 1996).

[3] R. N. Bracewell, *Two-Dimensional Imaging*, (Prentice-Hall, Englewood Cliffs, 1995).

[4] C. Cafforio, C. Prati, and F. Rocca, "SAR Data Focusing Using Seismic Migration Techniques," *IEEE Transactions on Aerospace and Electronic Systems*, vol. 27, pp. 194–207 (1991).

[5] R. Lanari and G. Fornaro, "A Short Discussion on the Exact Compensation of the SAR Range-Dependent Range Cell Migration Effect," *IEEE Transactions on Geoscience and Remote Sensing*, vol. 35, pp. 1446–1452 (1997).